A&A 676, A64 (2023)
https://doi.org/10.1051/0004-6361/202346144

Astronomy & Astrophysics
Special issue

Solar Orbiter First Results (Nominal Mission Phase)

Extreme-ultraviolet brightenings in the quiet Sun: Signatures in spectral and imaging data from the Interface Region Imaging Spectrograph★

C. J. Nelson[1,★★], F. Auchère[2], R. Aznar Cuadrado[3], K. Barczynski[4,5], E. Buchlin[2], L. Harra[5,4], D. M. Long[6,7], S. Parenti[2], H. Peter[3], U. Schühle[3], C. Schwanitz[5,4], P. Smith[6], L. Teriaca[3], C. Verbeeck[8], A. N. Zhukov[8,9], and D. Berghmans[8]

[1] European Space Agency (ESA), European Space Research and Technology Centre (ESTEC), Keplerlaan 1, 2201 AZ Noordwijk, The Netherlands
e-mail: chris.nelson@esa.int
[2] Université Paris-Saclay, CNRS, Institut d'astrophysique spatiale, 91405 Orsay, France
[3] Max Planck Institute for Solar System Research, Justus-von-Liebig-Weg 3, 37077 Göttingen, Germany
[4] ETH-Zurich, Wolfgang-Pauli-Str. 27, 8093 Zurich, Switzerland
[5] Physikalisch-Meteorologisches Observatorium Davos, World Radiation Center, 7260 Davos Dorf, Switzerland
[6] UCL-Mullard Space Science Laboratory, Holmbury St. Mary, Dorking, Surrey RH5 6NT, UK
[7] Astrophysics Research Centre, School of Mathematics and Physics, Queen's University Belfast, Belfast BT7 1NN, UK
[8] Solar-Terrestrial Centre of Excellence – SIDC, Royal Observatory of Belgium, Ringlaan 3 Av. Circulaire, 1180 Brussels, Belgium
[9] Skobeltsyn Institute of Nuclear Physics, Moscow State University, 11999 Moscow, Russia

Received 14 February 2023 / Accepted 8 June 2023

ABSTRACT

Context. Localised transient EUV brightenings, sometimes named 'campfires', occur throughout the quiet Sun. However, there are still many open questions about these events, in particular regarding their temperature range and dynamics.
Aims. We aim to determine whether any transition region response can be detected for small-scale extreme-ultraviolet (EUV) brightenings and, if so, to identify whether the measured spectra correspond to any previously reported bursts in the transition region, such as explosive events (EEs).
Methods. EUV brightenings were detected in a ∼29.4 min dataset sampled by the Solar Orbiter Extreme Ultraviolet Imager (EUI) on 8 March 2022 using an automated detection algorithm. Any potential transition region response was inferred through analysis of imaging and spectral data sampled through coordinated observations conducted by the Interface Region Imaging Spectrograph (IRIS).
Results. EUV brightenings display a range of responses in IRIS slit-jaw imager (SJI) data. Some events have clear signatures in the Mg II and Si IV SJI filters, whilst others have no discernible counterpart. Both extended and more complex EUV brightenings are sometimes found to have responses in IRIS SJI data. Examples of EUI intensities peaking before, during, and after their IRIS counterparts were found in light curves constructed co-spatial to EUV brightenings. Importantly, therefore, it is likely that not all EUV brightenings are driven in the same way, with some events seemingly being magnetic reconnection driven and others not. A single EUV brightening occurred co-spatial to the IRIS slit, with the returned spectra matching the properties of EEs.
Conclusions. EUV brightening is a term used to describe a range of small-scale events in the solar corona. The physics behind all EUV brightenings is likely not the same. More research is therefore required to assess their importance for global questions in the field, such as coronal heating.

Key words. Sun: activity – Sun: transition region – Sun: UV radiation

1. Introduction

Brightening events with sub-megameter scales and lifetimes of the order of minutes are seemingly ubiquitous throughout the solar atmosphere, from the photosphere to the corona, and from the quiet Sun to active regions. These events were first detected more than one century ago by Ellerman (1917), who identified transient intensity increases, now known as Ellerman bombs (EBs), in the wings of Hα line profiles sampled within an active region. Since then, a plethora of other classes of brightenings have been reported in the literature, including but not limited to explosive events (EEs; Brueckner & Bartoe 1983), blinkers (Harrison 1997), and UV bursts (Young et al. 2018), each with their own unique properties. The recent launches of satellites such as the Interface Region Imaging Spectrograph (IRIS; De Pontieu et al. 2014) and Solar Orbiter (Müller et al. 2020) have opened a new window into localised brightenings in the solar atmosphere, allowing us to probe the transition region and corona on unprecedented scales. These observational developments have led to an improved understanding of many events, such as IRIS bursts (Peter et al. 2014) and extreme ultraviolet (EUV) brightenings (Berghmans et al. 2021), thereby improving our understanding of energy release in the upper solar atmosphere. Importantly, coordinated observations between these two satellites have provided

★ Movies are available at https://www.aanda.org
★★ ESA Research Fellow.

the opportunity to understand the links between brightenings that are identified in different temperature windows, offering insights into the complex physics behind these events and their potential role in coronal heating (Cargill et al. 2015).

The detection of thousands of small-scale EUV brightenings (Berghmans et al. 2021), sometimes referred to as 'campfires', in quiet-Sun imaging data was one of the key early results of the Solar Orbiter Extreme Ultraviolet Imager (EUI; Rochus et al. 2020). These EUV brightenings have been shown to occur right down to the spatial resolution of EUI data sampled using the 17.4 nm High-Resolution Imager (HRI_{EUV}) telescope, at scales below what could have been routinely detected in data from the Solar Dynamics Observatory Atmospheric Imaging Assembly (SDO/AIA; Lemen et al. 2012). Although they were only discovered recently, these small-scale EUV brightenings have been widely studied by the community through both observations and numerical simulations. Zhukov et al. (2021), for example, combined imaging data sampled by SDO/AIA with data from HRI_{EUV} whilst Solar Orbiter was away from the Sun-Earth line. These authors used the distinct viewing angles of the two satellites to conduct stereoscopy of these events, finding that they typically form at heights between 1 Mm and 5 Mm in the solar atmosphere. Additionally, analysis of the line-of-sight photospheric magnetic field sampled by the SDO Helioseismic and Magnetic Imager (SDO/HMI; Scherrer et al. 2012) by Panesar et al. (2021) and the Solar Orbiter Polarimetric and Helioseismic Imager (PHI; Solanki et al. 2020) by Kahil et al. (2022) has shown that many (potentially around 70%) of these localised EUV brightenings occur co-spatial to bi-poles, where magnetic reconnection is thought to be possible. In addition, both numerical simulations (Chen et al. 2021) and magnetic field extrapolations (Barczynski et al. 2022) have supported the assertion that magnetic reconnection in the upper solar atmosphere could be driving these events.

One research area that is relatively unexplored relating to EUV brightenings identified in EUI data is whether they display spectral signatures across other temperature regimes of the atmosphere (e.g., in the chromosphere and transition region). Using imaging data sampled by SDO/AIA, both Panesar et al. (2021) and Dolliou et al. (2023) were able to identify that cool plasma was present in the lower solar corona co-spatial to some EUV brightenings, whilst Huang et al. (2023) studied the spectral response of three events in SPectral Imaging of the Coronal Environment (SPICE; SPICE Consortium 2020) data, finding responses in cooler lines for all studied events. However, whether a response to this plasma would be detected in the transition region for all events is currently unknown. If these EUV brightenings are driven by magnetic reconnection, then it is certainly plausible that they could form co-spatial and co-temporal to other burst signatures identified in observations sampling different temperature windows in the solar atmosphere. In the quiet Sun, this could include events such as photospheric quiet-Sun Ellerman-like brightenings (QSEBS; Rouppe van der Voort et al. 2016; Nelson et al. 2017) or transition region EEs (see Brueckner & Bartoe 1983; Huang et al. 2019). The coordinated observations conducted by HRI_{EUV} and IRIS during the first science orbit of Solar Orbiter (the EUI data are summarised in Berghmans et al. 2023) offer an ideal opportunity to assess the transition region response to these EUV brightenings and, therefore, to potentially better understand the effects of magnetic reconnection in the solar atmosphere.

In this article, we aim to further our understanding of small-scale EUV brightenings through analysis of data collected during coordinated observations between HRI_{EUV} and IRIS on 8 March 2022. Specifically, we aim to investigate whether signatures of these EUV brightenings are present in spectral and imaging data sampling transition region temperatures and, if so, whether these signatures match those of other well-known bursts (e.g., EEs). We structure our work as follows: We introduce the data we analysed in this article in Sect. 2. The results of our analysis are then presented in Sect. 3. A brief discussion is included in Sect. 4, before we draw our conclusions in Sect. 5.

2. Observations

We analyse a region of the quiet Sun observed by HRI_{EUV} using the 17.4 nm filter between 00:04:12 UT and 00:33:33 UT (all times have been converted into the reference frame of Earth) on 8 March 2022[1]. At 00:00:20 UT, the sub-solar point of Earth was 1.2° east and −3.0° south of the sub-solar point of Solar Orbiter, allowing coordination with Earth-bound observational infrastructure. The 2048 pixel × 2048 pixel images collected by HRI_{EUV} have a pixel scale of 0.492″, which, as Solar Orbiter was at a distance of approximately 0.49 AU from the Sun during this experiment, corresponds to approximately 174 km on the solar surface at disk centre. The cadence of images within this dataset was 3 s, and the exposure time was 1.65 s. We downloaded level-2 data from the Solar Orbiter Archive, with the identification of EUV brightenings being accomplished by employing the automated algorithm developed by Berghmans et al. (2021). This algorithm converted the original HRI_{EUV} data into Carrington coordinates (1 Carrington degree is equal to approximately 12.1 Mm on the solar surface), which involved a remapping of the images onto a 2172 pixel × 2172 pixel grid whilst maintaining the spatial sampling of each image. Following this, the properties of small-scale EUV brightenings distinct from the shot noise were extracted. Here, we analyse seven regions within the fields of view (FOVs) of both HRI_{EUV} and IRIS that were found to contain EUV brightening activity with sufficient areas and durations such that meaningful comparisons could be made between the instruments.

Whether any transition region response to the EUV brightenings could be detected was investigated using data sampled by the IRIS satellite. Between 00:04:20 UT and 00:34:09 UT, IRIS ran a dense eight-step raster with slit-jaw imager (SJI) intensity maps sampled by the 279.6 nm Mg II (temperature of $\sim 2 \times 10^4$ K) and 140 nm Si IV (temperature of $\sim 8 \times 10^4$ K) filters in sequence. These SJI data covered a FOV of 169″×175″ centred at heliographic coordinates of $x_c = -41''$, $y_c = 126''$, with pixel scales of 0.33″ (horizontal scale of 239 km) and cadences of 10 s. In addition to the SJI data, IRIS sampled spectra around several lines in the near- and far-ultraviolet, including C II 133.7 nm ($\sim 2 \times 10^4$ K), Si IV 139.4 nm ($\sim 8 \times 10^4$ K), Si IV 140.3 nm ($\sim 8 \times 10^4$ K), and Mg II k 279.6 nm ($\sim 10^4$ K). The raster data recorded for each spectral window had a spectral sampling of 0.005 nm, a raster step-size of 0.35″ (horizontal scale of 254 km), and a pixel scale along the slit of 0.33″. The time taken to sample the spectra at one raster position was 5 s, giving a total raster cadence of approximately 40 s and a total number of raster repeats of 44 during the experiment. The OBSID for this observational campaign was 3600607428.

Finally, we also studied co-spatial imaging and line-of-sight magnetic field data sampled by the SDO/AIA and SDO/HMI instruments, respectively. Our analysis of SDO/AIA data was limited to the 17.1 nm filter, which was primarily used for alignment purposes. These data have pixel scales of 0.6″ (435 km)

[1] EUI data release 5.0: https://doi.org/10.24414/2qfw-tr95

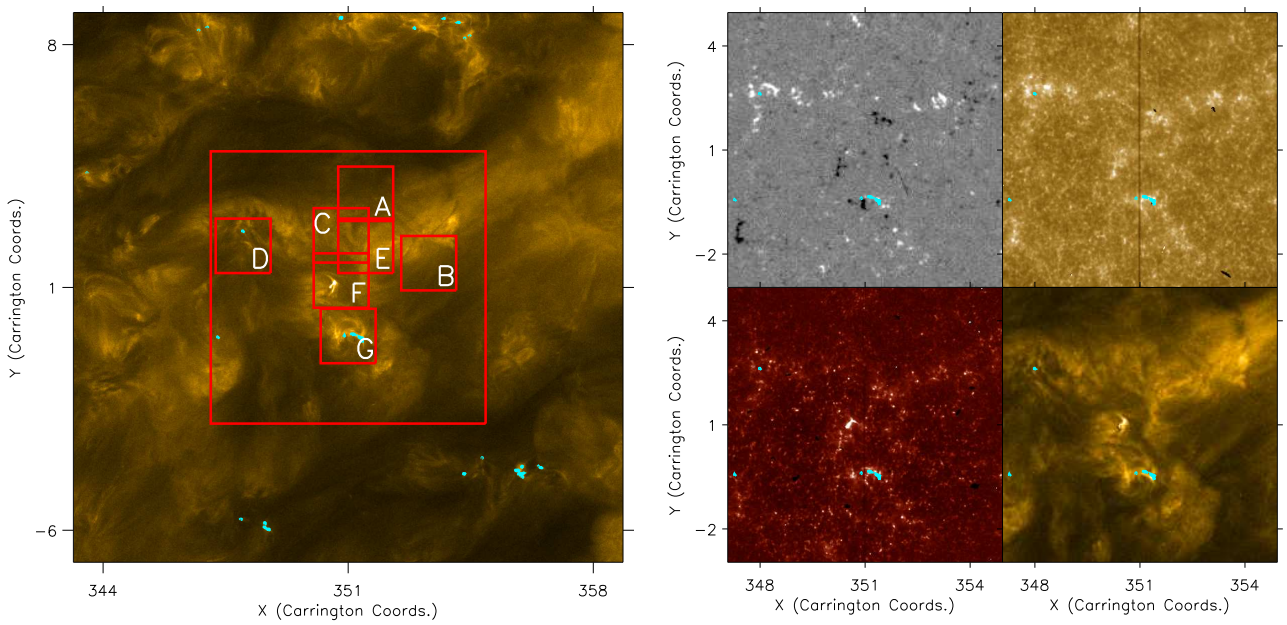

Fig. 1. Context image for the quiet-Sun region. In the left panel, we plot a zoom-in of the HRI_{EUV} FOV observed at 00:04:21 UT on 8 March 2022. The larger red overlaid box outlines the IRIS FOV plotted in the right panels, whilst the smaller, labelled red boxes (corresponding to approximately 19.1 Mm × 19.1 Mm) outline the sub-FOVs that contained the EUV brightening activity. In the right panels, we plot the IRIS FOV as sampled by SDO/HMI line-of-sight magnetograms (top left), the IRIS Mg II 279.6 nm filter (top right), the IRIS Si IV 140 nm filter (bottom left), and the SDO/AIA 17.1 nm filter (bottom right). The cyan contours indicate the locations of EUV brightenings identified in the plotted HRI_{EUV} frame.

and cadences of 12 s. The line-of-sight magnetic field maps collected by the SDO/HMI instrument have post-reduction pixel scales of 0.6″ (435 km) and cadences of 45 s. Basic alignment between instruments was conducted by converting the FOVs observed by HRI_{EUV}, IRIS, SDO/AIA, and SDO/HMI into Carrington coordinates at each time-step using the meta-data of each file. Closer alignments were completed by aligning local HRI_{EUV} and SDO/AIA 17.1 nm intensity maps around each studied EUV brightening as required. In Fig. 1 we plot the FOV studied here as sampled by each of these four instruments. The left panel plots an HRI_{EUV} image for a region around the IRIS FOV, which is indicated by the larger overlaid red box. The seven smaller, red boxes labelled A-G indicate the sub-FOVs that contained the EUV brightening activity analysed here. The right panels plot the region within the IRIS FOV (larger red box) for the photospheric line-of-sight magnetic field inferred by the SDO/HMI instrument (top left), the intensity in the chromospheric IRIS Mg II 279.6 nm filter (top right), the intensity in the transition region IRIS 140 nm Si IV filter (bottom left), and the intensity in the SDO/AIA 17.1 nm filter (bottom right). The locations of EUV brightenings identified in the plotted HRI_{EUV} frame are outlined by the cyan contours. The similarities between features in the HRI_{EUV} and SDO/AIA data indicates that our basic alignment is reasonable for general analysis. If we were instead to investigate the one-to-one relation between intensities at pixels within different instruments, then closer alignment and interpolations would be required.

3. Results

3.1. Elongated EUV brightenings with clear IRIS responses

3.1.1. Imaging response

We begin our analysis by investigating whether any chromospheric or transition region signatures could be detected co-spatial to EUV brightenings that were elongated and appeared to extend along a specific path (a behaviour that could potentially be described as jet-like) returned by the algorithm from HRI_{EUV} data. We identified seven events within regions D-F that matched this description, with durations of the order of several minutes. We note that this duration corresponds to the lifetime of any macro-structure containing EUV brightenings returned by the algorithm in the HRI_{EUV} data, rather than individually detected EUV brightenings from the algorithm, for reasons that we discuss in the next paragraph. In Fig. 2 we plot an example of an extended event that was found within region E. In the top row, we plot the intensity as sampled by HRI_{EUV} over the course of around 204 s. Initially, no EUV brightening is detected (first column) within this region before an event appears (cyan contour overlaid on the second column) that remains visible over the following 100 s (third and fourth columns) before fading from view (fifth column). The second and third rows plot the co-spatial and co-temporal responses of the IRIS Mg II 279.6 nm and Si IV 140 nm filters. No clear signature is present co-spatial to the EUV brightening (if we assume a good alignment) in the Mg II 279.6 nm images, but an extended structure is present in the Si IV 140 nm data. This localised event appears to extend slightly further south than the EUV brightening, and it remains visible after the HRI_{EUV} event is no longer apparent. No evidence of interactions, such as cancellation, between opposite-polarity magnetic fields is present in the SDO/HMI line-of-sight photospheric magnetic field maps (bottom row).

Although an off-set is apparent between the transition region and coronal brightening activity presented in Fig. 2, this is not a universal property. Six of the seven extended EUV brightening events have IRIS Si IV 140 nm signatures that appear to be perfectly co-spatial to the HRI_{EUV} structures, whilst only one (the event plotted in Fig. 2) is clearly offset (beyond any slight alignment errors). In Fig. 3 we plot an example of EUV brightening activity from region F, which displays a transition

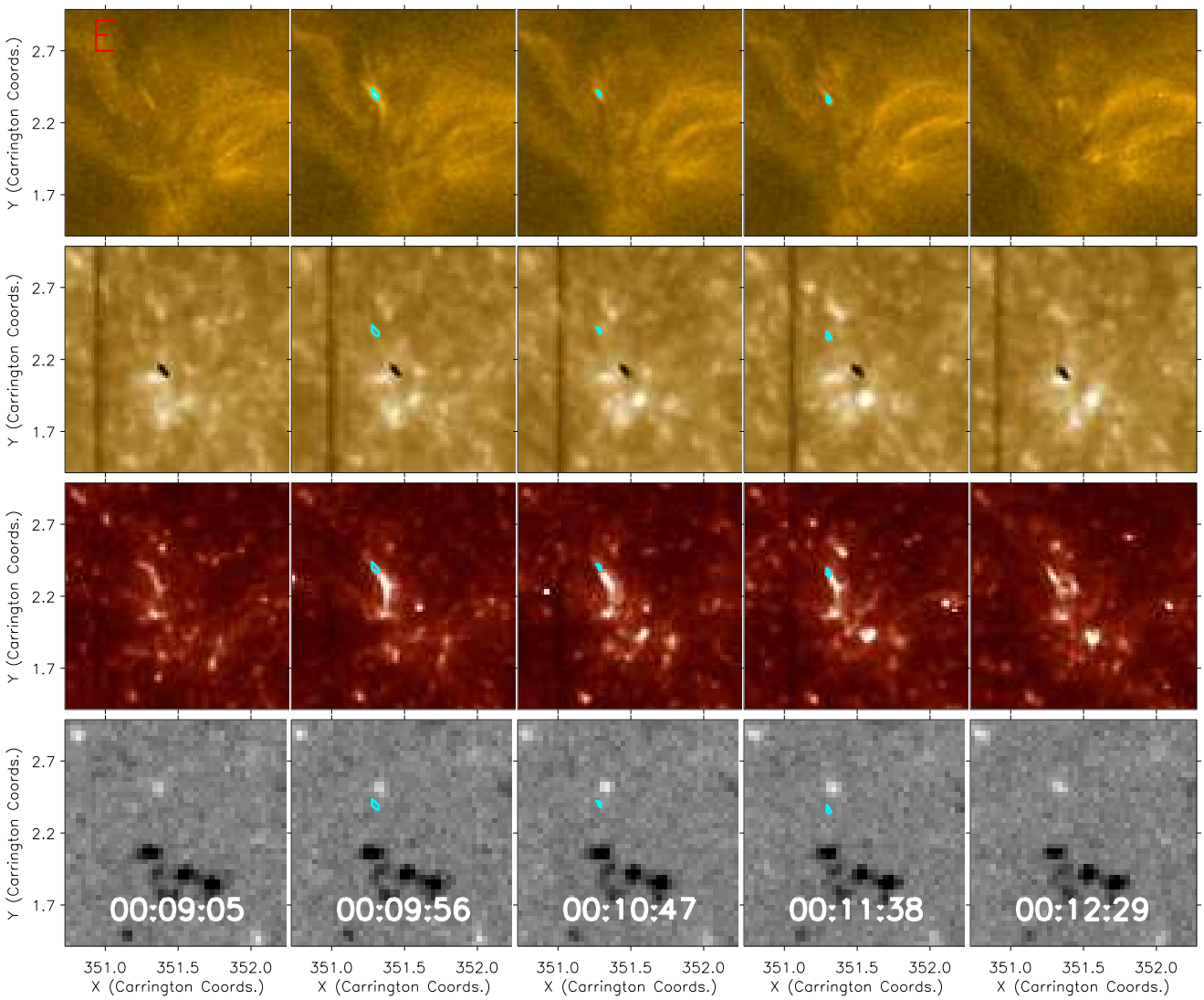

Fig. 2. Example of an extended EUV brightening from region E. The top row plots the HRI_{EUV} intensity at five time-steps over the course of around 204 s. The EUV brightening activity is outlined by the cyan contours. The second row plots the co-spatial and co-temporal IRIS Mg II 279.6 nm filter SJI response (the dark spot in the centre of the images is a known blemish in the filter), while the third row plots the equivalent, but for the Si IV 140 nm filter. A clear brightening is evident in the Si IV 140 nm channel with a similar shape to, but extending slightly further to the south from, the EUV brightening in the HRI_{EUV} data. The bottom row plots the line-of-sight photospheric magnetic field at this location as sampled by the SDO/HMI instrument. An animation of this region is available online.

region signature at the same spatial location over the course of around six minutes. Again, the top row plots the HRI_{EUV} intensity at this location, with the cyan contours outlining the EUV brightening detected by the algorithm. The lack of an automatically detected EUV brightening in the third column, where a bright macro-structure is present, explains our decision to discuss regions of EUV brightening activity rather than individual events. Once again, no obvious brightening is apparent in the IRIS Mg II 279.6 nm data, but a clear extended event is present in the Si IV 140 nm images. The transition region brightening appears to brighten slightly before the associated HRI_{EUV} brightening activity. No clear bi-poles are present in the photospheric line-of-sight magnetic field at these locations (fourth row). The fourth column shows that the IRIS slit passed directly through this EUV brightening, meaning that we are able to analyse its associated spectra below.

To further our analysis of these events, we also studied the temporal evolution of the intensities of extended EUV brightening activity in IRIS and HRI_{EUV} data. In Fig. 4 we plot normalised light curves constructed by summing the intensity in small boxes (around 1.8 Mm^2, the exact dimensions varied depending on the topology of the feature) around four regions of extended EUV brightening activity, selected from E and F, through time. The black lines plot the intensity sampled by HRI_{EUV}, and the EUV brightening activity is evident as intensity bumps of around 10–40% of the pre-brightening intensity. The blue and red lines plot the co-spatial and co-temporal IRIS Mg II 279.6 nm and Si IV 140 nm intensities, respectively, for each event. Clear increases in intensity (up to 70%) are apparent for each of these events in the Si IV 140 nm data, and the rightmost three of these also show Mg II 279.6 nm intensity increases (of up to 25%). The temporal evolution of these light curves is not the same for each extended EUV brightening. The HRI_{EUV} brightening occurs either 50 s before (first panel; corresponding to the event plotted in Fig. 2), co-temporally with (second panel), or between 100–150 s after (third and fourth panels;

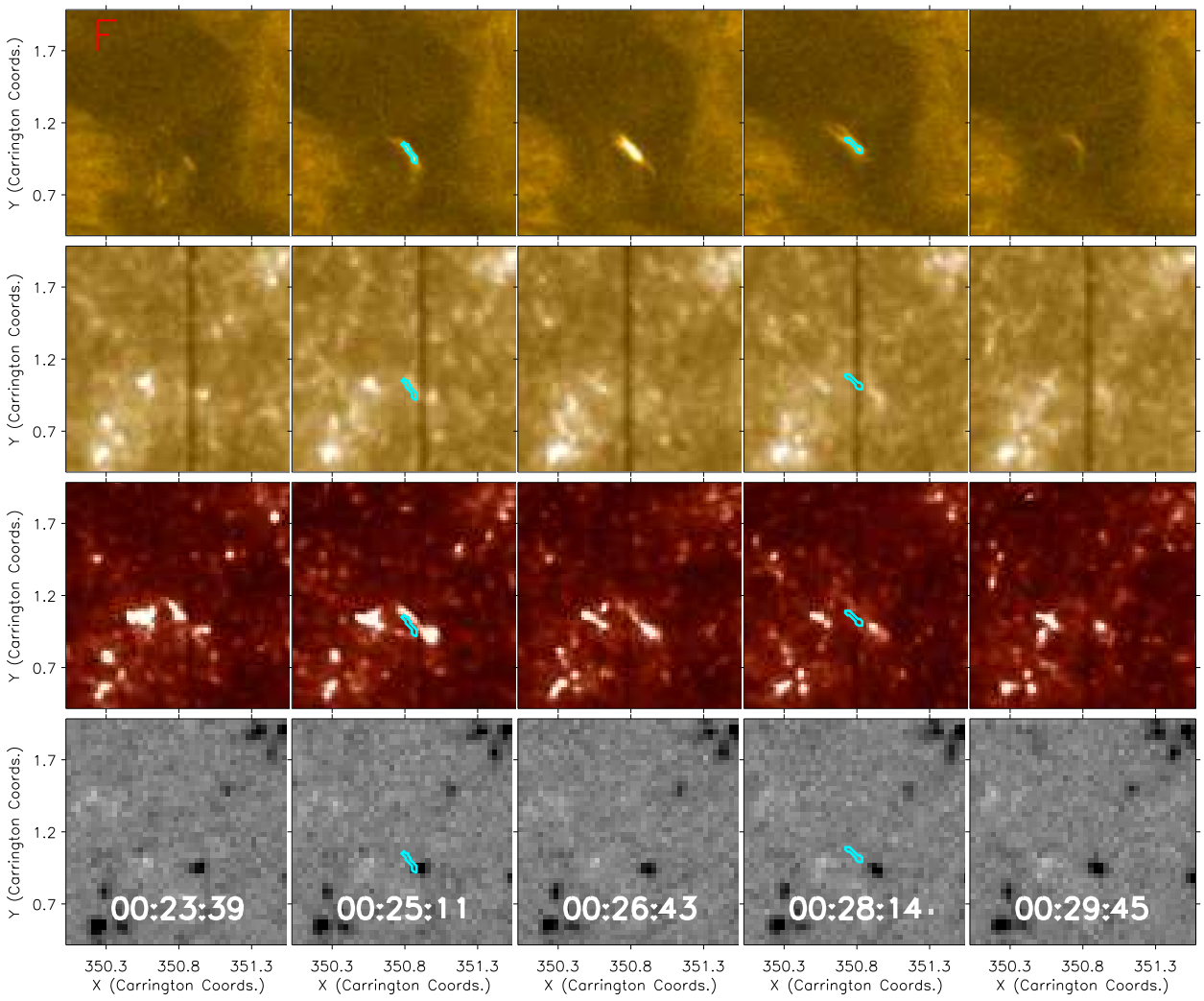

Fig. 3. Same as Fig. 2, but for an extended EUV brightening identified in region F. No large off-set (a small north-south off-set may be present) is apparent between this EUV brightening and the co-temporal IRIS Si IV 140 nm SJI response. The IRIS slit passed through this event during its occurrence, as can be seen clearly in the fourth column. An animation of this region is available online.

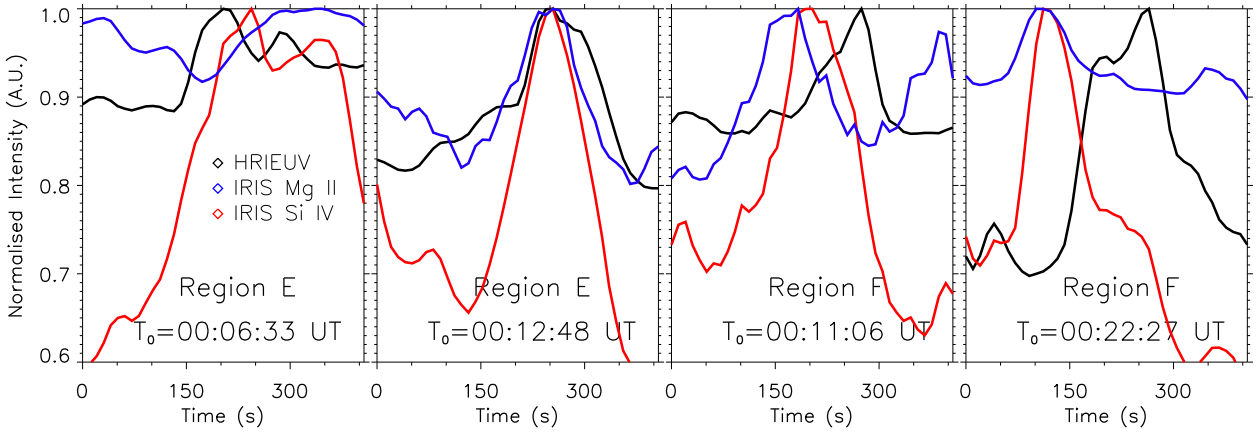

Fig. 4. Light curves of the mean intensity around four extended EUV brightening within regions E and F. The black lines plot light curves constructed from the HRI_{EUV} data, and the blue and red lines plot light curves constructed using the IRIS Mg II 279.6 nm and Si IV 140 nm SJI filters, respectively. The left two panels plot light curves constructed from small boxes (the sizes of which were close to 1.8 Mm^2, with the exact dimensions being varied to encompass the different orientations of individual EUV brightenings and any co-spatial associated brightenings in IRIS data) around two EUV brightenings within region E. The first panel corresponds to the event plotted in Fig. 2. The right two panels plot light curves constructed from small boxes (like those constructed for region E) around two EUV brightenings within region F. The fourth panel corresponds to the event plotted in Fig. 3. The HRI_{EUV} intensity is found to peak before (first panel), co-temporally with (second panel), and after (third and fourth panels) the IRIS Si IV SJI 140 nm SJI filter intensity for different events. Clear brightening events are also found in the Mg II 279.6 nm filters for the rightmost three of these four events. The time defined as $t = 0$ s is overlaid on each panel.

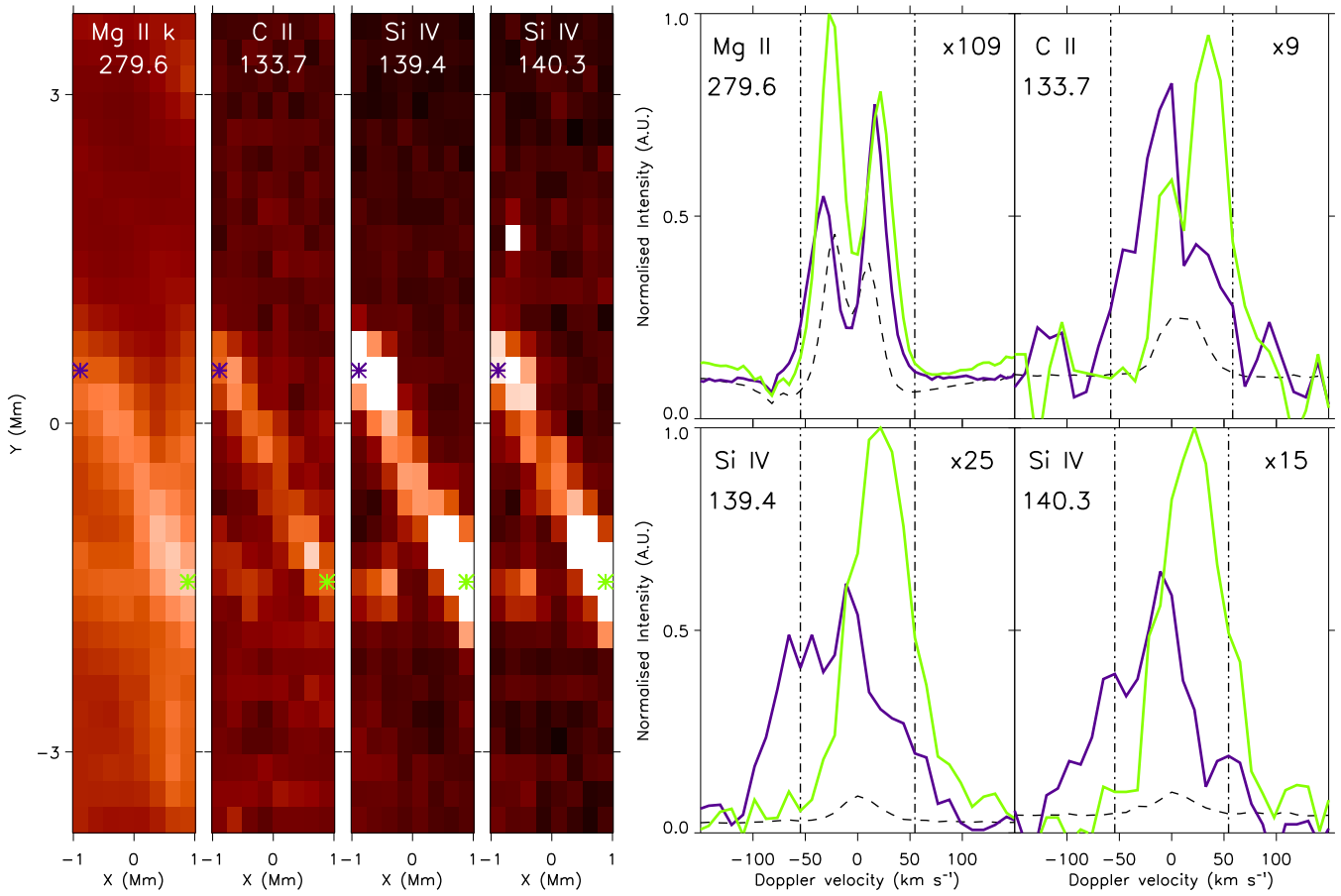

Fig. 5. Spectral response to the extended EUV brightening plotted in Fig. 3 as sampled at 00:25:21 UT. The left four panels plot the integrated intensity over 110 km s^{-1} Doppler velocity windows around the rest wavelength for the Mg II 279.6 nm (first panel), C II 133.7 nm (second panel), Si IV 139.4 nm (third panel), and Si IV 140.3 nm (fourth panel) spectral lines. The four panels on the right plot the spectra sampled at the positions of the coloured crosses in the left panels (within the first and last raster positions). The dashed black lines plot the average spectra calculated from this raster, whilst the two vertical dot-dashed lines book-end the Doppler velocity windows integrated across to construct the left panels. Each spectral profile has been normalised against the peak value (DN/s) from these three spectra. The normalisation factor is printed in the top right corner. The spectra are slightly blue-shifted (-22 km s^{-1}; calculated from a single-Gaussian fit to the Si IV 139.4 nm line) at the left side of the FOV (purple spectra), and they are slightly red-shifted (+22 km s^{-1}; calculated from a single-Gaussian fit to the Si IV 139.4 nm line) at the right side of the FOV (green spectra).

corresponding to the event plotted in Fig. 3) the associated IRIS intensity increases. Light curves constructed from the remaining three regions of extended EUV brightening activity were less clear because the intensity enhancements in both the HRI$_{EUV}$ and IRIS SJI filters were lower. They were therefore not plotted.

This range of results is difficult to explain through one model alone, with many sub-types of extended EUV brightenings appearing to be present. We discuss three specific examples. The first sub-type includes extended brightenings that are detected co-spatially and sequentially from cooler to hotter filters over the course of several minutes. These signatures could correspond, for example, to gradual heating of plasma from chromospheric to coronal temperatures caused by a single instance of energy release in the solar atmosphere or by the sequential release of energy at different layers of the solar atmosphere over this time-period. Other explanations are also possible. The second sub-type includes co-spatial extended brightenings where the intensity peaks co-temporally in all filters. Potential explanations for this include both a single instance of highly impulsive energy release heating relatively cool plasma to coronal temperatures almost instantaneously or the occurrence of rapid cooling, which is detected in many different temperature bands almost instantaneously. The third sub-type includes extended brightenings where an off-set is apparent for the structure in different filters and where the intensity in the hotter channels peaks before the intensity in the lower temperature channels. This sub-type implies that not all EUV brightenings returned by the algorithm indicate locations where heating is currently occurring in the solar atmosphere. At least some events returned by the algorithm indicate material that is in its cooling phase (presumably following an earlier heating event that may or may not have been detected, depending on its properties). The spatial off-sets between the structure in different filters could indicate that this specific event was not at all driven by magnetic reconnection. Instead it could be similar in nature to supersonic downflows that are driven by thermal instability (caused by coronal rain) that are regularly observed in the transition regions of sunspots (e.g., Nelson et al. 2020a,b). Movies depicting the temporal behaviour of the four regions studied in this sub-section are available online.

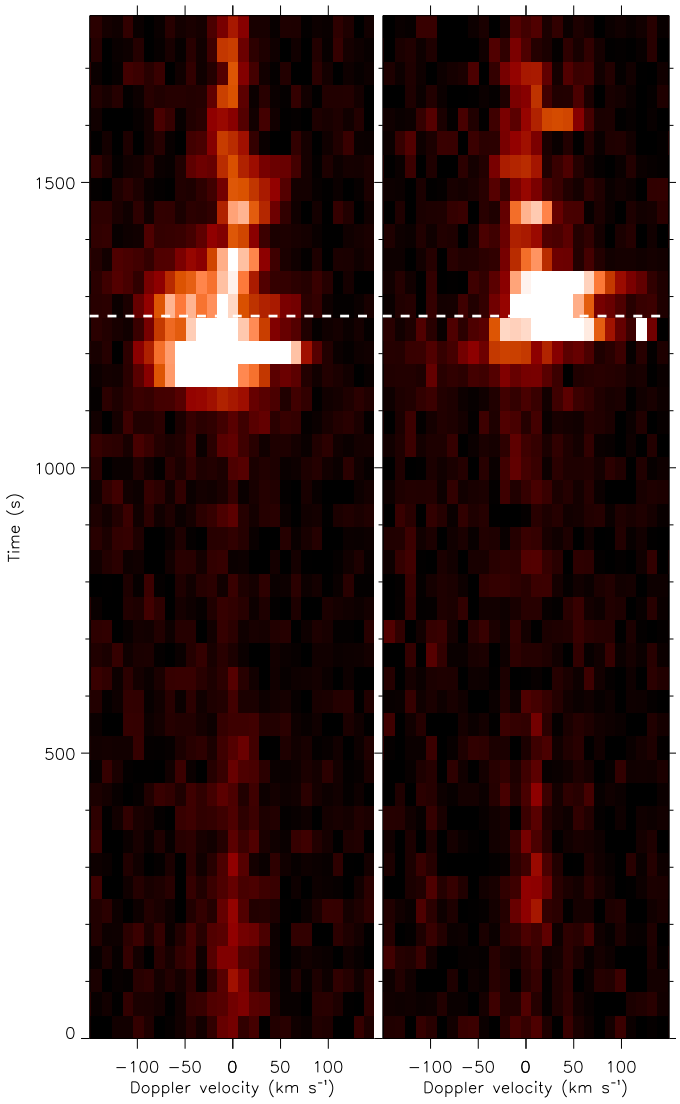

Fig. 6. Spectral-time maps constructed from the Si IV 139.4 nm line for the two pixels (the left panel corresponds to the purple crosses, and the right panel corresponds to the green crosses) plotted in Fig. 5. The dashed horizontal white lines indicate the time-step plotted in that figure. The clear blue- and red-shifts measured at either end of the EUV brightening from the spectra are evident at multiple time-steps throughout the evolution of this apparent EE.

3.1.2. Spectral response

To continue our investigation of extended EUV brightenings, we also analysed the spectra sampled co-spatial to the event plotted in Fig. 3. In the left four panels of Fig. 5, we plot the summed intensity across a 110 km s^{-1} Doppler window centred on the rest wavelengths of four spectral lines sampled by IRIS at 00:25:21 UT. A diffuse brightening is apparent in the Mg II k 279.6 nm image (first panel), but this is not as clear as the long thin brightening apparent in the C II 133.7 nm (second panel), Si IV 139.4 nm (third panel), and Si IV 140.3 nm (fourth panel) images. In the right panels, we plot spectra sampled at the locations of the coloured crosses (the colours of the crosses match the colours of the relevant lines) overlaid on the left images, normalised against the peak DN/s values from the three lines plotted in each panel. The dashed black line in each panel plots the average background spectra across the raster scan. Clearly, the intensity is increased at the locations of the EUV brightening for each line, with the spectra also being broader. Clear oppositely directed Doppler shifts are also apparent at the two ends of the extended structure. A velocity of −22 km s^{-1} is measured at the left edge of the raster (purple lines; from the Si IV 140.3 nm spectra using a single Gaussian fit), and a Doppler velocity of +22 km s^{-1} is measured at the right side of the raster (green lines). It is possible that these velocities correspond to reconnection outflows from a central energy-release location.

Studying the Si IV spectral windows in more detail allowed us to make further inferences about this extended EUV brightening event. For example, the intensity ratio between the Si IV lines was around 1.7 (see the normalisation factors printed in the top right corner of each spectral panel in Fig. 5) at both ends of the feature at multiple time-steps, indicating that this event may have been formed under optically thick conditions (see, for example, Mathioudakis et al. 1999). Additionally, no over-laid absorption lines (e.g., Ni II) were present on the Si IV 139.4 nm spectra indicating that this event was not an IRIS burst (the properties of which are described in, for example, Peter et al. 2014; Nelson & Kleint 2022a,b), which are only found in active regions (Kleint & Panos 2022). The lifetime, area, spectral shapes, and Doppler velocities of this event match the properties of EEs in the transition region well, however (see e.g., Teriaca et al. 2004; Huang et al. 2014, 2019). Unfortunately, no density measurements were possible within this EUV brightening, as there was not enough signal to identify the O IV 139.9 nm line above the noise level. Future work studying data collected with longer exposure times are required to investigate this further.

In Fig. 6 we plot spectral-time diagrams for the two pixel locations studied in detail in Fig. 5. The dashed horizontal white lines indicate the time-step plotted in that figure. The clear blue- and red-shifts at either end of the apparent EE are evident at multiple time-steps. A broadening of the spectra is apparent up to around ±100 km s^{-1}. Several other EUV brightenings were observed to occur close to the IRIS slit during this dataset, but this was the only example that displayed an unambiguous IRIS SJI response that could be traced through the spectra. Analysis of other features would require sub-pixel alignments between the two instruments across the FOV. We therefore stress that given the range of EUV brightening activity observed within this FOV, this result should not be interpreted as general to all such events. A larger statistical study must be completed to assess general EUV brightening transition region spectra in the near future.

3.2. Complex EUV brightenings with clear IRIS responses

In addition to extended structures, several examples of more complex EUV brightening activity are present within regions F-G. For a distinction to the previous subsection, and because the connectivity of these events is difficult to infer from imaging data alone, we simply refer to these events as 'complex'. In Fig. 7 we plot an example of a region of complex EUV brightening activity within region F at five time-steps. Initially, two small point-like EUV brightenings are detected in the HRI$_{EUV}$ data (first panel of the first row) before this expands to be five small distinct EUV brightenings in the second column (less than one minute later). After this, a period of rapid intensity increase occurs (third column) before several distinct spiral-like arms appeared (fourth column). Finally, this was followed by the occurrence of two extremely fast (>300 km s^{-1}) apparent jets propagating towards the top left and bottom right (the tip of this jet can be identified by the rightmost EUV brightening detected by the algorithm

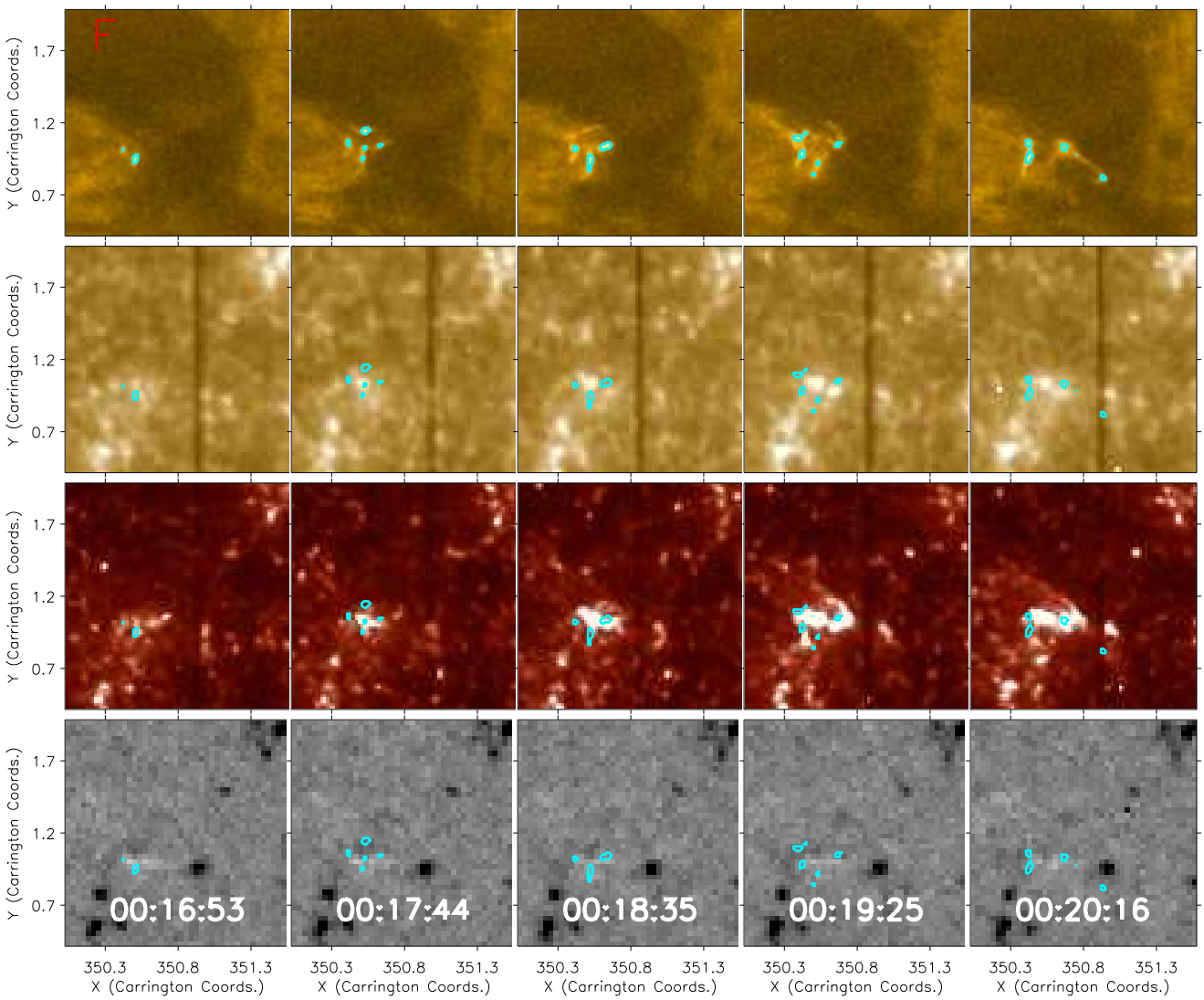

Fig. 7. Same as for Fig. 3, but for a more complex EUV brightening. Multiple small EUV brightenings are returned by the algorithm throughout this time in the HRI_{EUV} images, outlined by the cyan contours. A small point-like brightening develops in the Mg II channel co-spatial to the HRI_{EUV} activity, whilst a well-defined structure is evident in the Si IV filter. This structure includes two spiral arms that are most clearly observed in the fourth column. An animation of this region is available online.

in the fifth column) of the FOV. In the IRIS Mg II 279.6 nm channel (second row), a point-like brightening occurs (which is not morphologically similar to the features identified in the HRI_{EUV} data) during the third and fourth columns at the same spatial location as the grouping of EUV brightenings. The Si IV 140 nm data (third row), on the other hand, display similar spatial structuring as the HRI_{EUV} data. The spiral-like arms in the fourth column are clearer in the transition region image. The line-of-sight photospheric magnetic field does not display any evidence of cancellation, but the coronal dynamics support the hypothesis that magnetic reconnection is driving this complex EUV brightening activity. The presence of many automatically detected EUV brightenings across a small FOV also suggests that we may be resolving localised instances of energy release within the larger-scale (potential) magnetic reconnection event. The dynamics discussed here can be more clearly seen in the online movie.

Three further examples of complex EUV brightening activity that also displayed responses in the IRIS SJI data were present in these data. Two of these (one each in regions F and G) were evident in the first HRI_{EUV} frame, meaning that we were unable to study their full temporal evolutions, whilst the other occurred between 00:11 UT and 00:17 UT in region G. In Fig. 8 we plot light curves for the two regions of complex EUV brightening activity whose entire lifetimes were sampled. The left panel plots light curves constructed from a region (again around 1.8 Mm^2 in area) surrounding the event plotted in Fig. 7 and displays a single intensity peak that is co-temporal in both the IRIS SJI filters and the HRI_{EUV} data. The second region of complex EUV brightening activity displayed a more variable behaviour. Multiple different intensity peaks are detected in the IRIS SJI Si IV 140 nm data (red line) over the course of around three minutes. Only a single intensity peak was evident in the IRIS SJI Mg II 279.6 nm filter (blue line) and the HRI_{EUV} data (black line), and the Mg II response occurred during the decay phase of the HRI_{EUV} peak. Each of the intensity peaks in the IRIS SJI Si IV 140 nm filter manifests as small (diameters >2 Mm) bursts occurring at the same spatial location through time. Only one instance of brightening is apparent in the HRI_{EUV} imaging data. Owing to the complexity of this behaviour, it is not possible to offer

direct insights into the exact physical mechanisms occurring at this location.

3.3. EUV brightenings without clear IRIS responses

In the previous subsections, we analysed four regions (D-G) of EUV brightening activity where clear burst-like signatures were also present in IRIS imaging and, for one example, spectral data. We note, however, that this is not a one-to-one relation and that a number of EUV brightenings do not appear to display any transition region response. Specifically within this dataset, we identified four periods of EUV brightening activity within regions A-C that displayed no discernible response in the IRIS SJI data. In Fig. 9 we plot a clear example of an automatically detected EUV brightening, contained within a larger structure, for which no IRIS response was detected throughout its lifetime. The top row plots HRI_{EUV} images around the event with a cadence of approximately 101 s. Over these seven minutes, a long and thin structure with two perpendicular arms appears in the HRI_{EUV} images (most clearly seen in the third column). An EUV brightening is detected where the arms appear to meet (cyan contour). By the fourth column, a second vertically orientated arm had appeared, and a second EUV brightening was detected at the base of this. Neither the distinct arms of the larger structure nor the EUV brightening activity detected in the HRI_{EUV} data were discernible in the IRIS Mg II 279.6 nm or Si IV 140 nm filters (second and third rows, respectively). Additionally, the line-of-sight magnetic field did not display any clear evidence of a bi-pole, nor a cancellation at the location of this event (bottom row).

The other three example instances of EUV brightening activity within regions A-C that displayed no clear response in co-spatial and co-temporal IRIS imaging data were similar to the example plotted in Fig. 9 in that they were point-like regions (diameters of several pixels) with lifetimes of between one and four minutes. It is possible that these events correspond to an energy release in the upper solar atmosphere, where the plasma is already at temperatures above those sampled by the IRIS filters prior to the additional input of energy. However, given that these IRIS SJI data are summed spatially (i.e. the spatial sampling is twice the highest possible resolution), it is also possible that an IRIS response would have been present in higher-resolution data, but that it is unresolved here. This would need to be tested through an examination of unsummed IRIS SJI data collected during subsequent coordinated observations. Overall, we are not in a position to estimate the percentage of EUV brightenings that display an IRIS response due to our small sample size, but we are able to confirm that this value is non-zero. Movies depicting the EUV brightening activity in regions A-C, as well as the IRIS SJI Mg II 279.6 nm and Si IV 140 nm filter intensities, are available online.

4. Discussion

The discovery of EUV brightenings on extremely small scales (Berghmans et al. 2021) and their apparent links to magnetic reconnection (e.g., Chen et al. 2021; Kahil et al. 2022) has been one of the key early results of Solar Orbiter. We investigated whether signatures of EUV brightenings were evident in transition region imaging and spectral data sampled by the IRIS satellite. Through our analysis of seven distinct spatial regions (labelled A-G), we found that some but not all EUV brightenings display co-spatial and co-temporal responses in IRIS imaging data. Because the nature of the results obtained through our analysis is varied and complex, we provide a brief overview here and a summary in Table 1.

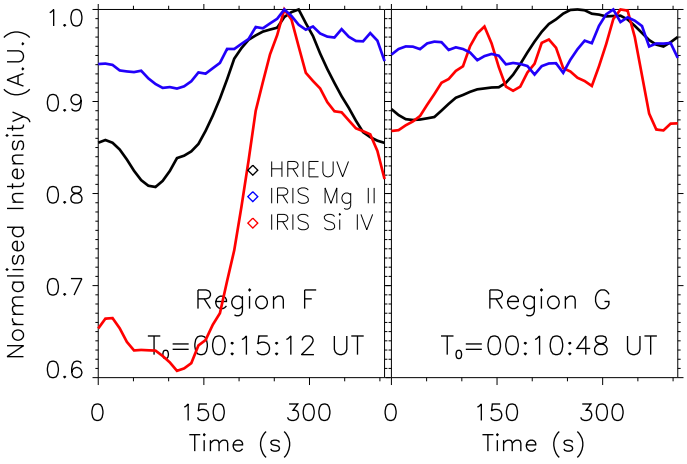

Fig. 8. Light curves of the mean intensity around two regions of complex EUV brightening activity within regions F (left panel) and G (right panel). Again, the black lines plot light curves constructed from the HRI_{EUV} data, and the blue and red lines plot light curves constructed using the IRIS Mg II 279.6 nm and Si IV 140 nm SJI filters, respectively. The left panel plots the light curves constructed from a small box (similar to those discussed in Fig. 4) around the event plotted in Fig. 7. The HRI_{EUV} intensity is found to peak co-temporally with the increased emission in both IRIS SJI filters for the left panel. For the right panel, however, several short bursts (lifetimes of the order of seconds) are evident in the IRIS Si IV 140 nm intensity during the occurrence of the EUV brightening. The time defined as $t = 0$ s is overlaid on each panel.

In regions D-G, we found seven instances of extended (long and thin structures; see Figs. 2 and 3) EUV brightening activity and four instances of more complex (rapidly evolving structures; see Fig. 7) EUV brightening activity co-spatial to brightenings in data sampled by the Si IV 140 nm SJI filter. Eight of these events also displayed signatures in the Mg II 279.6 nm filter, suggesting that EUV brightenings can occur across a range of temperature windows. In regions A-C, however, we found four instances of point-like EUV brightenings that displayed no co-spatial and co-temporal intensity increases in IRIS SJI data (see Fig. 9). Whether unsummed (in the spatial domain) IRIS SJI data would have returned a signature needs to be tested through an analysis of data sampled during other coordinated observations. Our small sample size does not allow us to infer any estimate for the overall number of EUV brightenings that display signatures in transition region imaging, but we are able to conclude that this number is non-zero.

Analysis of light curves, constructed from both HRI_{EUV} and IRIS SJI data, sampled co-spatial to EUV brightenings that displayed intensity increases in both, returned contrasting behaviour. For three events (both extended and complex), intensity increases were apparent in the IRIS imaging data between 100–150 s prior to the EUV brightening-related intensity increase in the HRI_{EUV} data, suggesting heating of the plasma from temperatures below 8×10^4 K (IRIS SJI Si IV 140 nm filter temperature response) to above 8×10^5 K (HRI_{EUV} temperature response). For two events, however, the intensity increases occurred co-temporally, potentially implying a single instance of energy release across multiple temperature ranges. Finally, for one example (plotted in Fig. 2), the HRI_{EUV} intensity increase occurred prior to the co-spatial brightening in the Si IV imaging data, potentially indicating that plasma cooling from

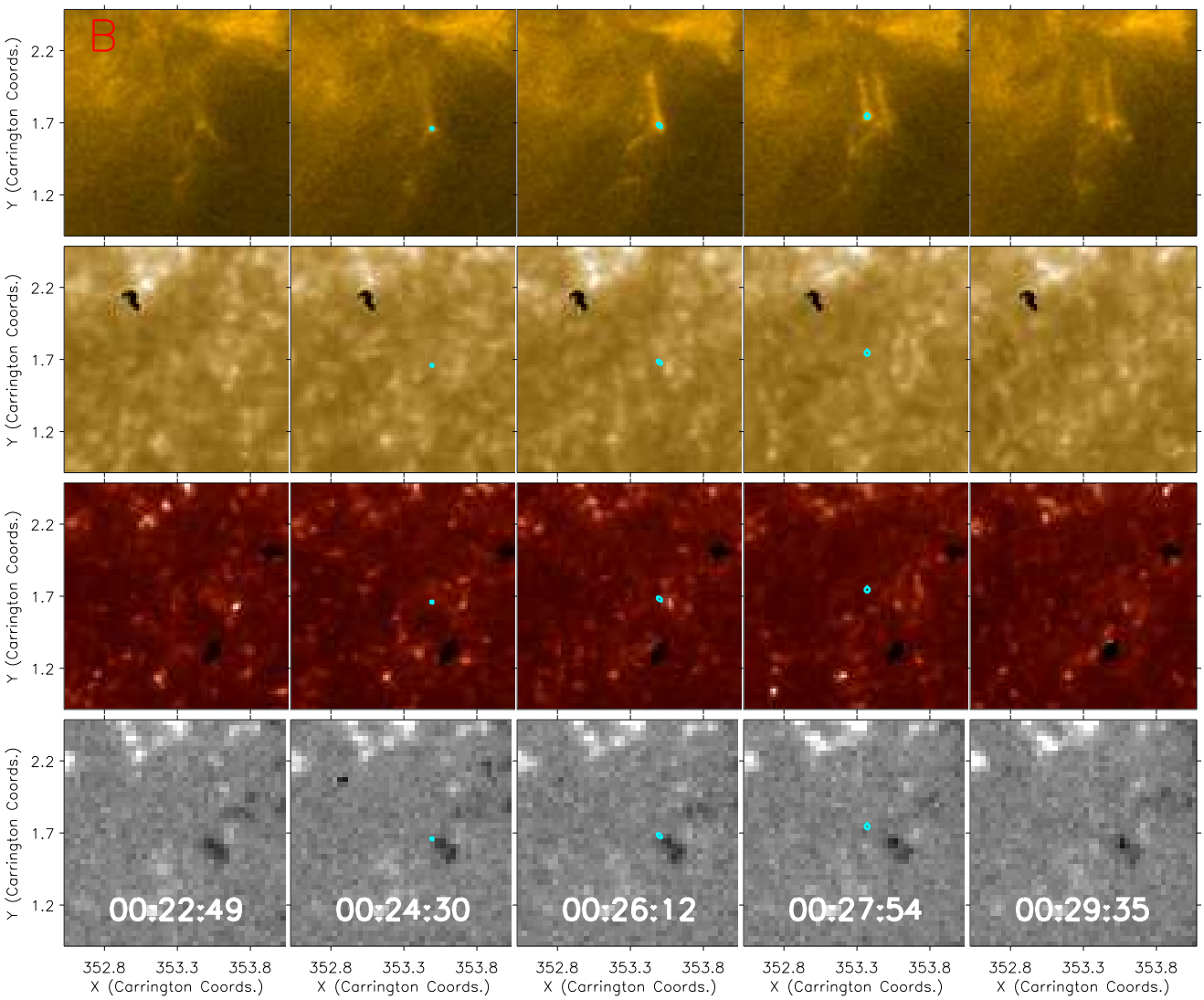

Fig. 9. Same as for Fig. 3, but for an EUV brightening without a signature in either IRIS SJI filter. A clear structure is evident in the HRI_{EUV} images. The automatically detected EUV brightening (outlined by the cyan contours) is detected where two almost perpendicular arms appear to meet. Neither the arms nor a transient point-like brightening at the location of the EUV brightening are apparent in the IRIS SJI filter data. An animation of this region is available online.

temperatures above 8×10^5 K to temperatures below 8×10^4 K could be causing the EUV brightening signature. The light curves constructed from the other EUV brightenings were inconclusive. These results imply that EUV brightenings (as returned by the algorithm) are not always evidence of current heating events. Some might indicate locations of plasma cooling through the HRI_{EUV} temperature passband. This could occur for several reasons, including but not limited to previous heating at the same location, which may have been too impulsive to be detected by instruments (Cargill 1994; Cargill et al. 2015; Parenti et al. 2019), or the occurrence of the thermal instability in a coronal loop leading to the detection of rapidly cooling plasma at the loop footpoints (Nelson et al. 2020a,b). We favour this second interpretation for the event reported in this article. The light curves discussed here can be found in Figs. 4 and 8.

Finally, we also analysed the spectral response of several lines sampled by IRIS co-spatial to an EUV brightening that occurred along the slit (see Figs. 3, 5 and 6). Both intensity increases and spectral broadening were evident in all of the Mg II k 279.6 nm, C II 133.7 nm, Si IV 139.4 nm, and Si IV 140.3 nm lines co-spatial to this event. Additionally, the ratio of the Si IV 139.4 nm and 140.3 nm lines was about 1.7, indicating that this event may have been formed under optically thick conditions, whilst oppositely directed Doppler shifts, with speeds of around 22 km s^{-1} were identified at either end of the EUV brightening. These combined results indicate that the transition region brightening co-spatial to the EUV brightening may be an EE (as discussed by e.g., Teriaca et al. 2004; Huang et al. 2014, 2019). Unfortunately, no density estimates were possible due to the short exposure times that returned low O IV intensities.

5. Conclusions

The situation we find here in terms of the thermal connectivity is somewhat reminiscent of that found previously for other similar phenomena. For example, spectroscopic time-series observations in the temperature minimum, chromosphere, and transition region show a comparably complex picture in that sometimes brightenings can be seen in purely one temperature domain, or simultaneously across two or three of these distinct temperature

Table 1. Summary of the 15 EUV brightenings.

Region	Event	Type	Mg II	Si IV	Co-spatial	Spectra	Feature	T_{START}(UT)	T_{END}(UT)	Bi-pole
A	1	Point	No	No	–	–	–	00:22:28	00:26:32	No
B	1	Point	No	No	–	–	–	00:08:14	00:12:18	Yes
B	2	Point	No	No	–	–	–	00:22:49	00:29:35	No
C	1	Point	No	No	–	–	–	00:27:03	00:29:45	No
D	1	Extended	No	Yes	Yes	–	–	00:12:08	00:15:31	No
D	2	Extended	No	Yes	Yes	–	–	00:20:16	00:23:39	No
D	3	Extended	No	Yes	Yes	–	–	00:25:31	00:27:33	No
E	1	Extended	No	Yes	No	–	–	00:09:05	00:12:29	No
E	2	Extended	Yes	Yes	Yes	–	–	00:15:21	00:18:45	No
F	1	Complex	Yes	Yes	–	–	–	00:04:20	00:08:24	Yes
F	2	Extended	Yes	Yes	Yes	–	–	00:14:20	00:16:22	Yes
F	3	Complex	Yes	Yes	–	–	–	00:16:22	00:22:28	Yes
F	4	Extended	Yes	Yes	Yes	Yes	EE	00:23:39	00:29:45	No
G	1	Complex	Yes	Yes	–	–	–	00:04:20	00:07:44	Yes
G	2	Complex	Yes	Yes	–	–	–	00:12:49	00:18:55	Yes

Notes. General information about the 15 EUV brightenings studied here, including the region in which they were identified; their label within that region; the type of EUV brightening; whether there was a response in the IRIS Mg II SJI data; whether there was a response in the IRIS Si IV SJI data; whether this response was co-spatial to the EUV brightening; whether IRIS spectra were available for the event; the type of spectra returned; the start of the temporal region of interest around the event; the end of the temporal region of interest around the event; and whether a (tentative) bi-pole was apparent in SDO/HMI data.

regions (Brković & Peter 2003). A clear example of this is how UV bursts and EBs can both occur individually or together (e.g., Vissers et al. 2015; Chen et al. 2019). In EBs, strong horizontal flows push together vertical magnetic field of opposite direction (in regions of high plasma-β), leading to very efficient reconnection low down in the solar atmosphere (Hansteen et al. 2017; Danilovic 2017). The co-formation of EBs and UV bursts can be explained by reconnection occurring at opposite ends of a long current sheet in response to emerging magnetic flux (Hansteen et al. 2019). For the events observed here (which appear to occur higher in the atmosphere), however, the question arises as to what might determine the different response of the plasma, in terms of transition region or coronal emission, to magnetic heating. EEs are typically modelled through reconnection of oppositely directed magnetic field in a low-β plasma (see e.g., Innes & Tóth 1999), which could hold for the EUV brightenings observed here. This raises the question of the role of plasma-β for these reconnection events (as discussed by Peter et al. 2019), and whether we might be able to find a unified reconnection picture for all these events and their thermal response at different temperatures.

Overall, our results indicate that there is no 'typical' response to EUV brightenings in the transition region, at least as observed by the IRIS imagers. Some events display clear co-spatial and co-temporal signatures, often with similar morphological properties, in Mg II and Si IV imaging data, whereas others display no detectable response at all. The spectral signatures of the single EUV brightening that could be confidently identified along the IRIS slit were comparable to EEs in the transition region (see e.g., Teriaca et al. 2004). Work analysing additional co-observations with IRIS sampled during future Solar Orbiter remote-sensing windows will allow us to make further inferences about the potential links between EUV brightenings and transition region events in the future.

Acknowledgements. CJN is thankful to ESA for support as an ESA Research Fellow. Solar Orbiter is a mission of international cooperation between ESA and NASA, operated by ESA. DML is grateful to the Science Technology and Facilities Council for the award of an Ernest Rutherford Fellowship (ST/R003246/1). SP acknowledges the funding by CNES through the MEDOC data and operations center. The EUI instrument was built by CSL, IAS, MPS, MSSL/UCL, PMOD/WRC, ROB, LCF/IO with funding from the Belgian Federal Science Policy Office (BELSPO/PRODEX PEA 4000134088, 4000112292, 4000136424, and 4000134474); the Centre National d'Etudes Spatiales (CNES); the UK Space Agency (UKSA); the Bundesministerium für Wirtschaft und Energie (BMWi) through the Deutsches Zentrum für Luft und Raumfahrt (DLR); and the Swiss Space Office (SSO). IRIS is a NASA small explorer mission developed and operated by LMSAL with mission operations executed at NASA Ames Research Center and major contributions to downlink communications funded by ESA and the Norwegian Space Centre. SDO/AIA and SDO/HMI data provided courtesy of NASA/SDO and the AIA and HMI science teams. This research has made use of NASA's Astrophysics Data System Bibliographic Services.

References

Barczynski, K., Meyer, K. A., Harra, L. K., et al. 2022, Sol. Phys., 297, 141
Berghmans, D., Auchère, F., Long, D. M., et al. 2021, A&A, 656, L4
Berghmans, D., Antolin, P., Auchère, F., et al. 2023, A&A, 675, A110 (SO Nominal Mission Phase SI)
Brković, A., & Peter, H. 2003, A&A, 406, 363
Brueckner, G. E., & Bartoe, J. D. F. 1983, ApJ, 272, 329
Cargill, P. J. 1994, ApJ, 422, 381
Cargill, P. J., Warren, H. P., & Bradshaw, S. J. 2015, Phil. Trans. R. Soc. London Ser. A, 373, 20140260
Chen, Y., Tian, H., Peter, H., et al. 2019, ApJ, 875, L30
Chen, Y., Przybylski, D., Peter, H., et al. 2021, A&A, 656, L7
Danilovic, S. 2017, A&A, 601, A122
De Pontieu, B., Title, A. M., Lemen, J. R., et al. 2014, Sol. Phys., 289, 2733
Dolliou, A., Parenti, S., Auchère, F., et al. 2023, A&A, 671, A64 (SO Nominal Mission Phase SI)
Ellerman, F. 1917, ApJ, 46, 298
Hansteen, V. H., Archontis, V., Pereira, T. M. D., et al. 2017, ApJ, 839, 22
Hansteen, V., Ortiz, A., Archontis, V., et al. 2019, A&A, 626, A33
Harrison, R. A. 1997, Sol. Phys., 175, 467
Huang, Z., Madjarska, M. S., Xia, L., et al. 2014, ApJ, 797, 88
Huang, Z., Li, B., & Xia, L. 2019, Sol.-Terr. Phys., 5, 58
Huang, Z., Teriaca, L., & Aznar Cuadrado, R. 2023, A&A, 673, A82 (SO Nominal Mission Phase SI)
Innes, D. E., & Tóth, G. 1999, Sol. Phys., 185, 127
Kahil, F., Hirzberger, J., Solanki, S. K., et al. 2022, A&A, 660, A143
Kleint, L., & Panos, B. 2022, A&A, 657, A132
Lemen, J. R., Title, A. M., Akin, D. J., et al. 2012, Sol. Phys., 275, 17
Mathioudakis, M., McKenny, J., Keenan, F. P., Williams, D. R., & Phillips, K. J. H. 1999, A&A, 351, L23

Müller, D., St. Cyr, O. C., Zouganelis, I., et al. 2020, A&A, 642, A1
Nelson, C. J., Freij, N., Reid, A., et al. 2017, ApJ, 845, 16
Nelson, C. J., & Kleint, L. 2022a, A&A, 668, A136
Nelson, C. J., & Kleint, L. 2022b, A&A, 666, A66
Nelson, C. J., Krishna Prasad, S., & Mathioudakis, M. 2020a, A&A, 640, A120
Nelson, C. J., Krishna Prasad, S., & Mathioudakis, M. 2020b, A&A, 636, A35
Panesar, N. K., Tiwari, S. K., Berghmans, D., et al. 2021, ApJ, 921, L20
Parenti, S., Del Zanna, G., & Vial, J. C. 2019, A&A, 625, A52
Peter, H., Tian, H., Curdt, W., et al. 2014, Science, 346, 1255726
Peter, H., Huang, Y. M., Chitta, L. P., & Young, P. R. 2019, A&A, 628, A8
Rochus, P., Auchère, F., Berghmans, D., et al. 2020, A&A, 642, A8
Rouppe van der Voort, L. H. M., Rutten, R. J., & Vissers, G. J. M. 2016, A&A, 592, A100
Scherrer, P. H., Schou, J., Bush, R. I., et al. 2012, Sol. Phys., 275, 207
Solanki, S. K., del Toro Iniesta, J. C., Woch, J., et al. 2020, A&A, 642, A11
SPICE Consortium (Anderson, M., et al.) 2020, A&A, 642, A14
Teriaca, L., Banerjee, D., Falchi, A., Doyle, J. G., & Madjarska, M. S. 2004, A&A, 427, 1065
Vissers, G. J. M., Rouppe van der Voort, L. H. M., Rutten, R. J., Carlsson, M., & De Pontieu, B. 2015, ApJ, 812, 11
Young, P. R., Tian, H., Peter, H., et al. 2018, Space Sci. Rev., 214, 120
Zhukov, A. N., Mierla, M., Auchère, F., et al. 2021, A&A, 656, A35